Nature Communications

https://doi.org/10.1038/s41467-026-73469-3

Article in Press

Cycling of Fe(II)/Fe(III) in the euphotic zone mediated by mineral photocatalysis

Received: 21 July 2025

Accepted: 12 May 2026

Cite this article as: Liu, T., Ding, H., Lu, A. *et al.* Cycling of Fe(II)/Fe(III) in the euphotic zone mediated by mineral photocatalysis. *Nat Commun* (2026). https://doi.org/10.1038/s41467-026-73469-3

Tong Liu, Hongrui Ding, Anhuai Lu, Lingzi Meng, Xiao Ge, Ying Liu, Fangchao Zhu, Shuo Yu, Qunjian Yin, Yan Li, Changqiu Wang, Juan Liu & Song Jin

Cycling of Fe(II)/Fe(III) in the euphotic zone mediated by mineral photocatalysis

Tong Liu[1,2#], Hongrui Ding[2#], Anhuai Lu[2,3*], Lingzi Meng[2], Xiao Ge[2], Ying Liu[2], Fangchao Zhu[3], Shuo Yu[3], Qunjian Yin[3], Yan Li[2], Changqiu Wang[2], Juan Liu[4], Song Jin[5]

[1] *State Key Laboratory of Regional and Urban Ecology, Research Center for Eco-Environmental Sciences, Chinese Academy of Sciences, Beijing 100085, China*

[2] *The Key Laboratory of Orogenic Belts and Crustal Evolution, Beijing Key Laboratory of Mineral Environmental Function, School of Earth and Space Sciences, Peking University, Beijing, 100871, China*

[3] *Key Laboratory of Tropical Marine Ecosystem and Bioresource, Fourth Institute of Oceanography, Ministry of Natural Resources, Beihai 536000, China*

[4] *The Key Laboratory of Water and Sediment Sciences, College of Environmental Sciences and Engineering, Peking University, Beijing 100871, China*

[5] *Department of Civil and Architectural Engineering and Construction Management, University of Wyoming, Laramie, WY 82071, USA*

# These authors contributed equally to this work.

* Corresponding author: Anhuai Lu

Email addresses: ahlu@pku.edu.cn

Abstract

The marine iron cycle is now recognized as fast and dynamic, partly fueled by vast particulate iron inputs. Yet the mechanisms that activate this reservoir to sustain productivity remain unresolved. Here we show that mineral photocatalysis, an overlooked abiotic process, provides a key activation pathway for Fe(II) production. Laboratory experiments using synthetic iron oxides and anatase in artificial seawater demonstrate that anatase (TiO_2) drives rapid Fe(III)-to-Fe(II) cycling at rates up to fourfold higher than current model assumptions. We propose this process explains the paradox of persistent Fe(II) in sunlit waters as a high-flux steady state of photochemical production coupled with biological uptake. Our findings establish mineral photocatalysis as a key driver in the ocean iron cycle, indicating that bioavailable iron fluxes from particles have been underestimated. Integrating photo-geochemical pathways into ocean models will improve predictions of iron recycling and ecosystem responses.

1. Introduction

Marine primary productivity is widely regulated by iron bioavailability [1]. Over the past decade, driven by the vast observational datasets from the GEOTRACES program and increasingly sophisticated global models, our understanding of the marine iron cycle has shifted from a slow, dust-dominated system to a highly dynamic, "fast" cycle [2]. This new framework recognizes a diverse portfolio of iron sources, where terrigenous inputs from continental margin sediments and hydrothermal vents rival or even exceed atmospheric dust on a global scale [3]. This places immense importance on understanding the fate of particulate iron phases, which can constitute 65% - 85% of the total iron inventory [4]. While this internal cycling of particles is known to meet >90% of biological demand in oligotrophic waters [5], and remains critical even in more productive regions [6], the fundamental physicochemical drivers that transform these vast, seemingly inert reservoirs into bioavailable forms remain a critical unresolved question in the new iron paradigm.

This knowledge gap is most acute when considering the paradoxical persistence of dissolved Fe(II) in surface waters [7]. Field measurements reveal that Fe(II) is consistently detectable throughout the euphotic zone across diverse ocean regions, from coastal waters to high-nutrient, low-chlorophyll (HNLC) areas, often forming subsurface maxima that persist on diel timescales despite oxidation half-lives of only minutes to hours [8,9]. As the form preferentially taken up by microorganisms [10], Fe(II) should be rapidly depleted by both remarkably fast biological uptake [11] and swift oxidation [12]. Prevalent explanations within oceanography, such as biological reduction [13–15] and organic photolysis [15], are insufficient to fully account for this sustained Fe(II) flux. Compounding this complexity, dissolved organic matter (DOM) and its associated Fe-complexing

ligands fundamentally govern iron speciation in seawater, stabilizing dissolved iron and modulating its photochemical reactivity and bioavailability. Fe(III) oxyhydroxides (ferrihydrite, lepidocrocite, goethite) and oxides (hematite) are major phases in both lithogenic and authigenic marine particles [4,16], and laboratory studies have long demonstrated their photo-reductive dissolution under UV–visible irradiation [17,18]. Crucially, these Fe(III) phases often co-occur with photoactive semiconductor minerals [19,20]. TiO_2 particles (primarily anatase) reach concentrations of 10^8 - 10^{10} particles L^{-1} in coastal waters, with decreasing gradients offshore [21,22]. Fe-oxide nanoparticles are ubiquitous in atmospheric dust and marine particulates globally [23,24], making their co-occurrence with anatase particularly prevalent in coastal marine environments.

This co-occurrence points to a critical oversight of abiotic pathways, a conclusion reinforced by the widespread presence of semiconductor minerals in marine suspended matter [23,24]. We hypothesize this missing link is a cornerstone of environmental photochemistry: the ability of semiconductor minerals to catalyze the photo-reductive dissolution of Fe(III) oxides. This process, first demonstrated decades ago in classic laboratory studies using synthetic minerals to elucidate fundamental mechanisms [18,25], has since been established as a driver of widespread photoelectric conversion and even microbial metabolism on the Earth's surface through studies incorporating both synthetic and natural minerals [12,26,27]. Yet, it has been largely overlooked in marine biogeochemical models, which have historically prioritized dissolved iron speciation while treating particles as passive carriers rather than reactive phases.

Herein, we provide direct experimental evidence for this overlooked process, investigating the role of anatase (TiO_2) as a model photocatalyst. Anatase is selected for three reasons: (i) its

widespread occurrence in marine particles [21,28]; (ii) its high photocatalytic activity under solar-spectrum irradiation [18]; and (iii) its favorable band alignment with Fe(III) oxides, which promotes efficient interfacial electron transfer [29,30]. Through a suite of controlled laboratory experiments, we demonstrate that anatase photocatalysis sustains a rapid Fe(III)-Fe(II) redox cycle at the mineral-seawater interface, dramatically enhancing the dissolution of common iron minerals. This mechanism produces bioavailable Fe(II) at rates exceeding direct photolysis, providing a mechanistic basis for the rapid internal cycling now recognized in the "fast iron" paradigm and offering a compelling explanation for the paradoxical persistence of Fe(II) within surface water. Once produced, Fe(II) can be taken up directly by microorganisms, support nitrogen fixation and sulfur oxidation, or be re-oxidized to Fe(III) phases, completing a rapid photochemical cycle that sustains iron bioavailability in the euphotic zone. Our findings establish mineral photocatalysis as a significant abiotic driver in the marine iron cycle, revealing that the reactivity of particulate iron is likely underestimated in current models [24,31,32]. This work calls for a re-evaluation of the drivers of marine iron bioavailability, integrating photo-geochemical processes into the next generation of ocean models.

2. Results

2.1. Photoactive semiconductors in marine particles

To characterize the environmental setting for our hypothesis, we selected the Beibu Gulf, a semi-enclosed bay in the northern South China Sea (China). This sunlit, shallow (average depth 60 m), and particle-rich system receives substantial terrestrial input from rivers like the Nanliu River, which contributes the highest sediment load regionally (average 0.11 kg m^{-3}, 2007 - 2020

[33]). To investigate the spatial variability of suspended minerals and their light-responsive properties, sampling sites spanned the bay, with emphasis on the Nanliu River estuary (Figure 1a, Supplementary Figure 1) to capture the influence of terrestrial mineral input. Estuarine waters exhibited significantly higher suspended particulate matter (SPM) concentrations (mean 4.5 mg L^{-1}) compared to offshore waters (mean 1.2 mg L^{-1}, Figure 1b), consistent with terrestrial runoff as a primary mineral source [34]. Vertical profiles revealed variable depth distributions: nearshore stations showed higher SPM concentrations near the bottom due to resuspension, while offshore stations exhibited relatively uniform profiles (Supplementary Figure 2). In both cases, substantial mineral loads persist within the euphotic zone, where light-driven processes can operate [35]. Analysis of the mineral composition (Figure 1c) shows that the suspended particles are a complex mixture. Although the bulk of the material consists of relatively inert clay minerals, this study focuses on investigating the photoactive components, iron and titanium oxides. These phases represent potential hotspots for photochemical cycling.

Raman spectroscopy revealed that suspended mineral particles are compositionally diverse but contain abundant semiconductor minerals including iron oxides (hematite) and titanium dioxide (anatase and rutile). Consistent semiconductor mineral assemblages were found in both the Beibu Gulf and its terrestrial source the Nanliu River (Supplementary Figure 3). This confirms the terrestrial origin of these key minerals [36]. Raman mapping analysis further revealed intimate spatial association of Fe- and Ti-bearing phases within individual particle aggregates (Figure 1d). We sought to determine if these natural particle assemblages possess intrinsic photoactivity (Figure 1e, f). Linear sweep voltammetry revealed a significant photocurrent generation by mineral electrodes:

light exposure enhanced the peak current by 87% compared to dark conditions, and yielded a 200% increase over blank fluorine-doped tin oxide (FTO) electrodes, reaching approximately 3.0 μA. Consistent with the semiconductor nature of iron oxides and titanium dioxide, chopped chronoamperometry confirmed negligible photo-response from non-semiconductor minerals like quartz and feldspar, while the photocurrent behavior of our mineral electrodes closely mirrored that of iron oxide mineral electrodes (Figure 1f). Crucially, in our experiments, acid washing to remove acid-soluble minerals (including metal oxides and sulfides [37]) substantially diminished the photoelectric effect (~60% reduction). This directly validates that the semiconductor mineral fraction, not the bulk silicate matrix, is the dominant source of the photoactivity of natural marine particulates. This co-location of abundant, photoactive mineral particles and sunlight in the surface ocean provides the essential conditions for the photocatalytic processes we detail in the following sections.

2.2. Anatase photocatalysis drives iron dissolution

In artificial seawater, light significantly enhanced Fe(II) release from synthetic iron oxyhydroxides, goethite, and lepidocrocite, demonstrating photochemical Fe(III) reduction. After 12 days, goethite exhibited a 16-fold increase in Fe(II) release under light (Figure 2a). Lepidocrocite showed even greater photoreduction, releasing 34% more Fe(II) than goethite under the same conditions. Both minerals approached apparent dissolution equilibrium after day 9, consistent with surface site saturation or product inhibition. These findings highlight the key role of photochemical Fe(III)/Fe(II) cycling in marine iron dynamics.

We next examined anatase's photocatalytic effect on synthetic Fe(III) minerals (ferrihydrite, lepidocrocite, goethite, and hematite); representative dissolution kinetics for lepidocrocite are shown in Figure 2b, c, with a comparative summary of ferrous content across all minerals presented in Figure 2d. The addition of anatase further amplified this photoreduction, leading to more pronounced increases in logarithmic growth rates: 4.8-, 2.1-, and 1.4-fold under light conditions by the end of the experiment (Figure 2b). Light and anatase together enhanced rates by 1.5 - 1.6-fold in overall Fe(II) release rates for ferrihydrite and lepidocrocite, and a 1.2-fold enhancement for hematite. This enhanced photoreduction was also evident in the dramatic shift towards Fe(II) speciation: Fe(II) proportions surged from approximately 10% - 15% in the dark to 35% - 60% under light exposure, across all four iron minerals (Figure 2d).

To simulate the influence of dissolved organic matter (DOM), oxalate (a model ligand that complexes Fe(III) and scavenges photogenerated holes) further amplified iron dissolution rates by over twofold compared to the light condition without oxalate, and further increased the Fe(II)/Fe(total) ratio (Figure 2d). These results demonstrate that DOM synergistically enhances iron bioavailability by both expanding the dissolved iron pool via complexation [38] and promoting anatase-assisted Fe(III) to Fe(II) photoreduction [39], consistent with the dominance of organic ligands in marine iron speciation [40], and may stabilize Fe(II) on particle surfaces [41]. Additional experiments with protocatechuic acid (PCA, an aromatic phenolic compound) and mixed oxalate-PCA ligands confirmed that all DOM types enhanced Fe(II) production under light and anatase, with magnitude varying as oxalate > mixed > PCA > no-DOM baseline (Supplementary Figure 4), demonstrating broad mechanistic applicability across DOM classes.

For comparison with models parameterized as fractional rates (% d^{-1}; e.g., PISCES [10]), we converted concentration-based Fe(II) release rates (μmol L^{-1} d^{-1}) to an equivalent fractional rate by normalizing to the initial solid-phase Fe inventory added in each experiment (calculated from mineral loading and Fe content). It is worth noting that photochemical iron dissolution rates in the presence of anatase in our study were up to ~40-fold higher than values used in current models (e.g., ~0.01% d^{-1} for particulate Fe photolysis in PISCES [10]). For instance, lepidocrocite exhibited equivalent fractional Fe(II) release rates of 0.06% d^{-1} (dark) and 0.43% d^{-1} (light + anatase), a >7-fold increase under illumination (Figure 2b). Hematite also showed a substantial enhancement, from 0.02% d^{-1} (dark) to 0.28% d^{-1} (light + anatase), a >10-fold increase. This suggests that current biogeochemical models may underestimate the contribution of photochemical processes to marine iron cycling. The dominant Fe(II) speciation observed under combined light-anatase conditions, further amplified by DOM components like oxalate, refines our understanding of iron speciation dynamics in seawater and the flux of bioavailable iron from particles. This pathway of rapid, light-driven Fe(II) production suggests that the observed picomolar Fe(II) concentrations in the ocean may reflect a dynamic steady state of much higher turnover than currently assumed in models.

High-resolution X-ray photoelectron spectroscopy (XPS) of lepidocrocite revealed a characteristic Fe(II) peak at 715.2 eV after reaction (Figure 2f), confirming photochemical Fe(III) reduction [42,43], a mechanism also reported in TiO_2-ferrihydrite systems [44]. Reflectance spectra (Figure 2e, Supplementary Figure 5) showed typical iron oxide photoexcitation transitions and a new peak at 520 nm emerged upon light exposure, indicating lepidocrocite structural transformation and the formation of anatase-lepidocrocite heterojunctions [17]. These photocatalytic

processes can also drive iron mineral phase transformations. While literature reports indicate that anatase-assisted photoelectron injection induces the transformation of lepidocrocite into more electronically favorable iron oxides such as hematite [44], our TEM-FFT analysis (Supplementary Figure 6) directly captured the transformation of ferrihydrite into goethite during the reaction. Both transformations represent progressions from metastable iron minerals toward thermodynamically more stable phases, with goethite serving as a widely recognized intermediate in iron oxide transformation pathways. The intimate heterojunction interfaces observed between goethite and anatase provide direct structural evidence for efficient charge separation [29,30]. These phase transformations are conceptually summarized in Figure 2g.

Taken together, these results demonstrate that anatase-catalyzed photoreactions provide an efficient pathway for the transformation and dissolution of terrigenous iron minerals, which are often considered chemically stable [10]. In contrast to the slow dissolution of authigenic iron oxides [16], these photo-induced processes substantially alter both the phase and electronic structure of the primary iron minerals. This enhanced charge separation efficiency ultimately leads to a substantial increase in dissolved iron concentrations, particularly the more bioavailable Fe(II) form [45], revealing a new source of reactive iron in sunlit surface waters.

2.3. Linking photocatalysis to microbial metabolism

To isolate microbial responses from direct light effects, we employed an electrochemical system where applied cathodic potentials serve as a controlled proxy for photogenerated electrons. In mineral photocatalysis, light absorption promotes electrons to the semiconductor conduction band,

making them available for microbial utilization; the applied potentials systematically vary this electron flux, enabling quantitative investigation of microbial metabolic responses.

Bacterial biomass correlated with applied potential, with optimal growth observed at approximately -0.3 V (vs. Ag/AgCl reference electrode) (Figure 3a). This simulated photoelectron-rich environment altered the bacterial community composition, selectively enriching genera such as *Alteromonas* and *Pseudoalteromonas* at more negative potentials, while *Halomonas* maintained higher relative abundance under open circuit potential conditions (Supplementary Figure 7). While prolonged exposure to this simplified system reduced overall microbial diversity, a pattern commonly observed in laboratory enrichments under strong selective pressure [46], the implications for complex natural marine systems require further investigation. In this electrochemical system, more negative cathodic potentials supply a greater flux of reductive electrons that directly reduce Fe(III) to Fe(II), thereby increasing Fe(II) availability; this approach mimics the photoelectrons generated during mineral photocatalysis. Complementary experiments with direct iron amendments also reshaped microbial community structure, favoring iron-utilizing microorganisms (Supplementary Figure 8). Elevated iron response in nearshore communities compared to offshore assemblages have been reported in other coastal systems [47], consistent with local adaptation to higher and more variable metal loads. Collectively, these findings suggest that the generation of photoelectrons and the subsequent increase in iron availability can act as selective factors, shaping microbial community structure and favoring populations adapted to redox-active environments, a process consistent with field observations where iron availability acts as a key driver of phytoplankton natural selection and metabolic remodeling [48].

The isolated strain *Halomonas* sp. exhibited significantly enhanced nitrate reduction rates and efficiency when exposed to simulated photoelectrons (Figure 3b), accompanied by notable shifts in nitrate reduction products (Supplementary Figure 9). Specifically, cultures at -0.2 V showed the lowest residual nitrate concentrations, though all applied potentials significantly differed from controls. Consistent with this enhanced metabolic activity, the activity of its electron transfer system (ETSA) was significantly elevated (Figure 3e), increasing markedly by day 10 under more negative potentials before partially declining by day 20. The concurrent increase in cytochrome *c* (Cyt *c*) content (Figure 3f), a key component for extracellular electron transfer [49], suggests that microorganisms upregulated their electron transfer capacity in response to the photoelectron-enriched environment, consistent with enhanced mineral-microbe interfacial interactions. Morphologically, SEM images also confirmed the response of cells to photoelectrons, with the formation of extracellular polymeric substances (EPS) and membrane vesicles observed under optimal growth potential (Supplementary Figure 10). Supporting these physiological observations, transcriptomic analysis revealed coordinated upregulation across multiple functional gene categories under applied potentials, including extracellular electron transfer (EET)-related genes, energy metabolism genes, nitrogen metabolism genes (e.g., *nasA*, *nasD*, *nirD*, *nosZ*), and biofilm-related genes, with the most pronounced responses observed at more negative potentials (Supplementary Figure 11). These results provide evidence that photoelectrons can substantially boost energy metabolism and drive accelerated nitrate reduction in this model organism, and presumably in other microbes.

To further investigate the synergistic effects of co-occurring minerals, we studied nitrate reduction by *Bacillus tropicus* in the presence of both anatase and lepidocrocite (under the same illumination conditions as the abiotic experiments: 300 - 800 nm, 100 mW cm^{-2}) (Figure 3c). The anatase-lepidocrocite combination exhibited the highest nitrate reduction efficiency, exceeding both anatase-only and mineral-free controls (Figure 3c), demonstrating a synergistic effect. This synergy likely arises from multiple electron transfer pathways, including direct utilization of photoelectrons by the microorganism and enhanced iron cycling promoted by the anatase-lepidocrocite interaction [50]. TEM analysis provided microscopic evidence for this synergistic effect (Supplementary Figure 12), the synthetic lepidocrocite and anatase particles added in the experiment were uniformly distributed around the *Bacillus tropicus* cells and were closely bound to their surfaces. This intimate contact enables efficient mineral-microbe electron transfer. Extending beyond nitrogen cycling, our experiments also showed that simulated photoelectrons and Fe(II) can influence broader microbial metabolic processes. For instance, sulfate-reducing bacteria demonstrated significantly higher sulfate reduction rates under applied photoelectron potentials (Figure 3d), suggesting potential impacts on element cycling in marine sediments.

To bridge our laboratory findings with real-world marine environments, we conducted extensive field observations in the Beibu Gulf, linking the distribution of suspended particulates to patterns of phytoplankton biomass. Spatial analysis revealed markedly elevated concentrations of chlorophyll a (reaching 2 - 5 mg m^{-3}) in coastal regions (Figure 3g), particularly near the Nanliu River estuary with a high mineral load [33], compared to offshore waters (<0.5 mg m^{-3}). Phytoplankton distribution in coastal systems is governed by multiple factors including nutrient

inputs and hydrodynamics [51]. However, the spatial co-occurrence we observed between high suspended particulate matter (Figure 1b) and high chlorophyll-a concentration (Figure 3g) provides an environmental context: the mineral-rich river plumes coincide with phytoplankton blooms. Similar patterns have been reported in other coastal systems, where seasonal mineral influx has been associated with variability in coastal chlorophyll-a, though the relationship reflects the interplay of multiple environmental factors [52,53]. Our DOM and optical analyses further confirmed biological signatures in these same coastal waters (Supplementary Figure 13).

3. Discussion

Building on the consensus that the marine iron cycle is rapid, our study pinpoints a key internal activation pathway. Recent work has highlighted large particulate-iron fluxes from continental margins and hydrothermal vents [3], yet the mechanisms that render these particles bioavailable remain unclear. We identified mineral photocatalysis as a previously overlooked pathway that transforms particulate iron into bioavailable Fe(II) at rates far exceeding those assumed in current models [10,31,32]. We recognize that our experimental conditions, surface-equivalent irradiance and pure mineral assemblages at elevated loadings, represent a mechanistic upper bound, whereas model parameterizations integrate across all particle types, depths, and irradiance regimes. The order-of-magnitude discrepancy nonetheless suggests that local photocatalytic rates in sunlit, mineral-rich waters may be substantially higher than global-mean values imply. This discovery provides an important abiotic pathway that not only helps resolve the long-standing paradox of

Fe(II)'s persistence in sunlit waters but also offers a physicochemical driver for the rapid internal cycling of iron.

Our findings refine the prevailing view of iron limitation in the oceans. The efficiency of this pathway suggests that low picomolar Fe(II) concentrations may not reflect limited supply. Instead, they likely represent a high-flux steady state, where photocatalytic production is tightly coupled with equally rapid consumption by marine biota. Under typical euphotic zone conditions, uncomplexed Fe(II) oxidizes within minutes to hours [54,55]. Our results therefore imply that sustained Fe(II) pools thus require continuous regeneration, which mineral photocatalysis can provide. Indeed, recent studies have highlighted the unexpectedly high iron uptake rates by picophytoplankton, which can be further enhanced by light. These studies underscore the high biological demand that drives the "ferrous wheel" [11]. Thus, "iron limitation" may denote not a meagre input, but a dynamic equilibrium between intense biological demand and equally rapid regeneration. The bioavailable iron flux from particles may thus be larger and more variable than recognized.

Our field observations in the Beibu Gulf provide an environmental context for these laboratory findings: the co-occurrence of high SPM and chlorophyll a (Figure 3g) is consistent with, though not proof of, a photocatalytic contribution in particle-rich euphotic zones. We emphasize that this coastal system is not classically Fe-limited; we selected it as a mineralogical analogue favoring mechanistic study. Our field sampling targeted bulk mineralogy and particle properties rather than dissolved Fe speciation; accordingly, our observations provide environmental context rather than direct Fe(II) flux quantification. The relevance to Fe-limited open-ocean regions remains to be

quantified, but several factors suggest the process may still contribute: atmospheric dust and lateral margin transport supply TiO_2 and Fe-oxide nanoparticles to remote waters [3,23], and even modest Fe(II) fluxes can be ecologically significant where demand far exceeds supply. Targeted field campaigns with trace-metal-clean Fe(II) measurements will be essential to test these predictions.

We synthesize these findings into a conceptual model of mineral photocatalysis in the euphotic zone (Figure 4). The environmental relevance is supported by the documented abundance of photoactive minerals in coastal waters [21,22]. Photo-catalytically active minerals thus serve three critical functions: (1) expanding the bioavailable iron pool through enhanced dissolution, (2) acting as a conduit for electron transfer to microorganisms, and (3) catalyzing the reduction of key electron acceptors such as nitrate and sulfate. As illustrated in Figure 4, terrigenous and atmospheric inputs supply semiconductor minerals that, under solar irradiation, generate bioavailable Fe(II) to fuel phytoplankton uptake, complete the Fe redox cycle, or serve as electron donors for microbial metabolisms, consistent with Fe(II)-driven denitrification in sediments [56] and direct photoelectron utilization by microbes [57]. Thus, mineral photocatalysis converts relatively inert particulate iron into a reactive intermediate modulating multiple elemental cycles.

Quantifying the relative importance of these interconnected pathways in diverse marine environments is a critical next step. The real ocean is far more complex. For instance, the role of DOM is multifaceted. While our experiments with oxalate and protocatechuic acid showed a synergistic enhancement, different DOM fractions can either enhance photocatalysis by acting as hole scavengers or inhibit it by blocking reactive sites [58]. The interplay between mineral surfaces and newly identified, marine-derived biogenic ligands [40] is an important frontier. Furthermore, the

specific mineralogy matters. Our work highlights the high efficiency of the anatase-iron oxide pairing, explained by favorable band alignment that promotes electron transfer [29,30]. We note that our experiments employed synthetic minerals with well-defined properties, which facilitates mechanistic interpretation but may not fully capture the complexity of natural particles. Natural marine particles are heterogeneous aggregates where semiconductor phases are often intimately mixed with clays and organic coatings [4]. While our photoelectrochemical measurements on natural Beibu Gulf particles (Figure 1e, f) confirm that such assemblages retain substantial photoactivity, the effective photocatalytic rates *in situ* will depend on factors such as mineral surface area, aggregation state, light penetration depth, and temperature, as warming accelerates Fe(II) oxidation kinetics while potentially altering photocatalytic efficiency.

In summary, our results identify mineral photocatalysis as a previously overlooked abiotic pathway in the marine iron cycle. We show that ubiquitous semiconductor minerals, particularly anatase coupled with Fe(III) oxides, can sustain rapid Fe(III)-Fe(II) cycling under realistic light and seawater conditions, at elevated rates in global biogeochemical models. Current models struggle to reproduce observed iron distributions, partly due to uncertainties in parameterizing internal cycling [31]; our findings suggest a specific, mineral-based process that could help fill this gap. In particle-rich coastal systems, mineral photocatalysis offers a physicochemical explanation for sustained Fe(II) fluxes that are tightly coupled to biological uptake. In Fe-limited open-ocean regions, analogous mechanisms may operate at lower intensities but could nonetheless modulate ecosystem productivity at critical thresholds. We therefore propose that mineral photocatalysis should be considered alongside biological reduction and organic photolysis as a key internal source

of bioavailable iron. Incorporating this process into ocean models may improve ecosystem predictions under environmental change [48], and may open new avenues for understanding how mineral-surface photochemistry governs the biogeochemical fate of other redox-sensitive elements in the global oceans.

4. Methods

4.1. Seawater sampling and particle characterization

Seawater samples were collected from the Yangtze River Estuary, Beibu Gulf (northern South China Sea, China), and coastal waters surrounding Hainan Island (Supplementary Figure 1). Cruises were conducted aboard R/V Haike 68 in summer (July - August 2023). Sampling stations were distributed across the bay with a focus on the Nanliu River estuary to capture the influence of terrestrial mineral input (Figure 1a, Supplementary Figure 1). Seawater was collected using a CTD-rosette system equipped with 12-L Niskin bottles (Seabird, US). At each station, water samples were collected from multiple depths within the euphotic zone (surface, 5 m, 10 m, and near-bottom where applicable).

Suspended particulate matter (SPM) concentration was determined gravimetrically following established protocols [59]. Seawater samples were filtered through pre-weighed 0.7 μm glass fiber filters (Whatman GF/F) immediately on board. Filters were rinsed with ultrapure water to remove sea salt, individually stored in acid-cleaned polystyrene petri dishes, and kept frozen at -20℃ until shore-based analysis. Upon return to the laboratory, filters were freeze-dried (-50℃, 24 h) and weighed using a calibrated analytical balance (Mettler Toledo XPR).

Mineral phase composition was analyzed by confocal Raman microscopy (Renishaw inVia Reflex) using a 532 nm laser (laser power 5 mW, acquisition time 10 s, spectral range 100 - 1800 cm^{-1}). Mineral phases were identified by comparison with the RRUFF database [60]. Morphological characterization and elemental mapping were performed by environmental scanning electron microscopy with energy-dispersive X-ray spectroscopy (ESEM-EDS, FEI Quanta FEG 450) at an accelerating voltage of 20 kV. Optical properties were measured using a UV-Vis-NIR spectrophotometer with an integrating sphere (Shimadzu UV-3000) for diffuse reflectance measurements in the 200 - 800 nm range, with $BaSO_4$ as the white reference standard [61]. Field sampling was designed for bulk mineralogical characterization and suspended particulate matter analysis; trace-metal-clean protocols for dissolved Fe or Fe(II) speciation measurements were not implemented in this campaign. Detailed procedures for all characterizations are provided in Supplementary Information.

4.2. Photocatalytic experiments

All iron minerals (ferrihydrite, lepidocrocite, goethite, hematite) and anatase nanoparticles used in photochemical experiments were synthetic. Iron minerals were synthesized following established protocols [62]; anatase nanoparticles (99.8% purity, 25 nm average particle size) were purchased from Sinopharm, China. Detailed synthesis procedures and characterization data (XRD, TEM, Raman, BET surface area) are provided in Supplementary Sections 1.3 and 1.4 and Supplementary Figure 5.

Batch photoreduction experiments were conducted in 50 mL quartz vials under simulated sunlight (solar simulator with AM 1.5G filter; 300 - 800 nm, 100 mW cm^{-2}, comparable to midday subtropical coastal irradiance). Iron minerals (0.5 g L^{-1}) and anatase (0.1 g L^{-1} where applicable) were dispersed in artificial seawater. Artificial seawater was prepared following [63]: NaCl 23.926 g, Na_2SO_4 4.008 g, KCl 0.677 g, $NaHCO_3$ 0.196 g, KBr 0.098 g, H_3BO_3 0.026 g, NaF 0.003 g, $MgCl_2 \cdot 6H_2O$ 10.831 g, $CaCl_2$ 1.102 g, $SrCl_2 \cdot 6H_2O$ 0.025 g per liter, sterilized by autoclaving (121℃, 20 min). Sodium oxalate (200 μM, Sinopharm Chemical Reagent Co., China) was used as a model DOM ligand in selected experiments. Samples were incubated at 25 ± 1℃ under light or dark (aluminum foil-wrapped) conditions for up to 12 days.

Fe(II) concentration was measured using the ferrozine assay [64]. Total dissolved iron was determined after Fe(III) reduction with hydroxylamine hydrochloride [64] and verified by ICP-AES (Thermo Scientific iCAP 7400) for selected samples [65]. For comparison with models parameterized as fractional rates (% d^{-1}; e.g., PISCES), we converted concentration-based Fe(II) release rates (μmol L^{-1} d^{-1}) to an equivalent fractional rate as $k(\%\, d^{-1}) = 100 \times (d[Fe^{2+}]/dt)/Fe_{solid,0}$, where $Fe_{solid,0}$ is the initial solid-phase Fe inventory added. Detailed analytical protocols are provided in Supplementary Information.

4.3. Microbial culture experiments

Halomonas sp. (previously isolated from the Yellow Sea euphotic zone [66]) and *Bacillus tropicus* (newly isolated from the Beibu Gulf during the summer 2023 cruise) were used as model marine bacteria for electrochemical and photocatalytic experiments. Indigenous microbial consortia from

Beibu Gulf surface waters were collected for community-level experiments. To assess iron's impact on native communities, Beibu Gulf consortia were incubated in artificial seawater amended with Fe(II) (1 μM added as $FeCl_2 \cdot 4H_2O$) for 14 days, with subsamples collected for 16S rRNA gene amplicon sequencing (Supplementary Section 1.6).

The metabolic response of *Halomonas* sp. to simulated photoelectrons was examined in a two-chamber photoelectrochemical (PEC) system with cathode potentials poised at -0.2, -0.3, and -0.4 V (vs. Ag/AgCl reference electrode), with open circuit potential (OCP) as control. We monitored growth (OD_{600}), nitrate reduction products, and transcriptomes (RNA-Seq, Supplementary Sections 1.6).

Bacillus tropicus was cultured under illumination (300 - 800 nm, 100 mW cm^{-2}) in artificial seawater with synthetic lepidocrocite (0.5 g L^{-1}) alone or combined with anatase (0.1 g L^{-1}). Sulfate-reducing bacterial (SRB) enrichment cultures from Beibu Gulf sediments were assessed under electrochemical potentials in the PEC system. Sulfate reduction was monitored by ion chromatography [67].

Key parameters were quantified using standard methods: bacterial abundance by spectrophotometry (OD_{600}); electron transfer system activity (ETSA) by INT reduction assay [68]; cytochrome c content by difference spectra [69]. Detailed protocols for microbial isolation, culture media, PEC system configuration, Fe(II) stock preparation, analytical procedures, RNA-Seq, and bioinformatics are provided in Supplementary Sections 1.6.

4.4. Data analysis and statistics

Data analysis and statistical tests were performed using R software [70]. Data normality was assessed using the Shapiro-Wilk test; non-parametric tests were applied to non-normally distributed data. Statistical significance was assessed using Student's t-tests or ANOVA with post-hoc Tukey tests, as appropriate, with a significance threshold of $p < 0.05$. Pearson correlation coefficients were calculated to evaluate correlations between variables. Error bars represent standard deviation unless otherwise stated.

Data Availability

All data supporting the findings of this study are available within the paper and its Supplementary Information. Tabular source data for figures are provided as Supplementary Data files. Sequencing data are available on the NCBI Sequence Read Archive (SRA) under accession number PRJNA565622. Bathymetric and topographic data used for map generation were obtained from the publicly available GEBCO_2023 global gridded bathymetric dataset (https://www.gebco.net). Any additional data are available from the corresponding author upon request.

Reference

1. Elrod, V. A., Berelson, W. M., Coale, K. H. & Johnson, K. S. The flux of iron from continental shelf sediments: a missing source for global budgets. *Geophys. Res. Lett.* **31**, (2004).
2. Tagliabue, A. & Weber, T. Novel insights into ocean trace element cycling from biogeochemical models. *Oceanography* **37**, 131–141 (2024).
3. Conway, T. M., Middag, R. & Schlitzer, R. Geotraces: Ironing out the details of the oceanic iron sources? *Oceanography* **37**, 35–45 (2024).
4. Boyd, P. W., Ellwood, M. J., Tagliabue, A. & Twining, B. S. Biotic and abiotic retention, recycling and remineralization of metals in the ocean. *Nat. Geosci.* **10**, 167–173 (2017).
5. Boyd, P. W. *et al.* FeCycle: attempting an iron biogeochemical budget from a mesoscale SF6 tracer experiment in unperturbed low iron waters. *Glob. Biogeochem. Cycles* **19**, (2005).
6. Tagliabue, A. *et al.* The interplay between regeneration and scavenging fluxes drives ocean iron cycling. *Nat. Commun.* **10**, 4960 (2019).
7. Bowie, A. R., Achterberg, E. P., Sedwick, P. N., Ussher, S. & Worsfold, P. J. Real-time monitoring of picomolar concentrations of iron(II) in marine waters using automated flow injection-chemiluminescence instrumentation. *Environ. Sci. Technol.* **36**, 4600–4607 (2002).
8. Croot, P. L. *et al.* Regeneration of Fe(II) during EIFeX and SOFeX. *Geophys. Res. Lett.* **35**, 2008GL035063 (2008).
9. Sarthou, G. *et al.* Labile Fe(II) concentrations in the atlantic sector of the southern ocean along a transect from the subtropical domain to the weddell sea gyre. *Biogeosciences* **8**, 2461–2479 (2011).
10. Aumont, O., Ethé, C., Tagliabue, A., Bopp, L. & Gehlen, M. PISCES-v2: an ocean biogeochemical model

for carbon and ecosystem studies. *Geosci. Model Dev.* **8**, 2465–2513 (2015).

11. Strzepek, R. F., Latour, P., Ellwood, M. J., Shaked, Y. & Boyd, P. W. Microbial competition for iron determines its availability to the ferrous wheel. *ISME J.* **19**, wraf015 (2025).
12. Lu, A. *et al.* Photoelectric conversion on earth's surface via widespread Fe- and Mn-mineral coatings. *Proc. Natl. Acad. Sci.* **116**, 9741–9746 (2019).
13. Aflenzer, H. *et al.* Effect of dissolved iron (II) and temperature on growth of the southern ocean phytoplankton species fragilariopsis cylindrus and phaeocystis antarctica. *Polar Biol.* **46**, 1163–1173 (2023).
14. Lampe, R. H., Coale, T. H., McQuaid, J. B. & Allen, A. E. Molecular mechanisms for iron uptake and homeostasis in marine eukaryotic phytoplankton. *Annu. Rev. Microbiol.* **78**, (2024).
15. Salmon, T. P., Rose, A. L., Neilan, B. A. & Waite, T. D. The FeL model of iron acquisition: nondissociative reduction of ferric complexes in the marine environment. *Limnol. Oceanogr.* **51**, 1744–1754 (2006).
16. Sofen, L. E. *et al.* Authigenic iron is a significant component of oceanic labile particulate iron inventories. *Glob. Biogeochem. Cycles* **37**, e2023GB007837 (2023).
17. Borer, P., Sulzberger, B., Hug, S. J., Kraemer, S. M. & Kretzschmar, R. Wavelength-dependence of photoreductive dissolution of lepidocrocite (γ-FeOOH) in the absence and presence of the siderophore DFOB. *Environ. Sci. Technol.* **43**, 1871–1876 (2009).
18. Hoffmann, M. R., Martin, S. T., Choi, W. & Bahnemann, D. W. Environmental applications of semiconductor photocatalysis. *Chem. Rev.* **95**, 69–96 (1995).
19. Bower, D. M., Hummer, D. R., Steele, A. & Kyono, A. The Co-evolution of Fe-oxides, Ti-oxides, and other microbially induced mineral precipitates In sandy sediments: understanding the role of cyanobacteria In weathering and early diagenesis. *J. Sediment. Res.* **85**, 1213–1227 (2015).

20. Fitzpatrick, R. W., Roux, J. L. & Schwertmann, U. Amorphous and crystalline titanium and iron-titanium oxides in synthetic preparations, at near ambient conditions, and in soil clays. *Clays Clay Miner.* **26**, 189–201 (1978).

21. Li, G. *et al.* Detection, distribution and environmental risk of metal-based nanoparticles in a coastal bay. *Water Res.* **242**, 120242 (2023).

22. Ying, S. *et al.* Location-dependent occurrence and distribution of metal-based nanoparticles in bay environments. *J. Hazard. Mater.* **476**, 134972 (2024).

23. Oakes, M., Weber, R., Lai, B., Russell, A. & Ingall, E. Characterization of iron speciation in urban and rural single particles using XANES spectroscopy and micro X-ray fluorescence measurements: investigating the relationship between speciation and fractional iron solubility. *Atmospheric Chem. Phys.* **12**, 745–756 (2012).

24. Tagliabue, A. *et al.* The integral role of iron in ocean biogeochemistry. *Nature* **543**, 51–59 (2017).

25. Fujishima, A. & Honda, K. Electrochemical photolysis of water at a semiconductor electrode. *Nature* **238**, 37–38 (1972).

26. Lu, A. *et al.* Growth of non-phototrophic microorganisms using solar energy through mineral photocatalysis. *Nat. Commun.* **3**, 768 (2012).

27. Lu, A., Li, Y. & Jin, S. Interactions between Semiconducting Minerals and Bacteria under Light. *Elements* **8**, 125–130 (2012).

28. Sun, Y. *et al.* Mineral composition and photochemical reactivity of suspended particulate matters in the euphotic zones of china's nearshore and estuarine regions. *Minerals* **13**, 552 (2023).

29. Kodan, N., Agarwal, K. & Mehta, B. R. All-oxide α-Fe_2O_3 /H:TiO_2 heterojunction photoanode: a platform for stable and enhanced photoelectrochemical performance through favorable band edge alignment. *J. Phys.*

Chem. C **123**, 3326–3335 (2019).

30. Xie, J. *et al.* Highly selective oxidation of methane to methanol at ambient conditions by titanium dioxide-supported iron species. *Nat. Catal.* **1**, 889–896 (2018).

31. Tagliabue, A. *et al.* How well do global ocean biogeochemistry models simulate dissolved iron distributions? *Glob. Biogeochem. Cycles* **30**, 149–174 (2016).

32. Rogerson, J. J. Not all models are created equal: assessing parameterisations of iron dynamics in ocean biogeochemical models. (University of Cape Town, 2020).

33. Li, S. *et al.* Variations in the Suspended Sediment Concentration in Mountain-Type Rivers Flowing Into the Sea in the Past 60 years—Taking Nanliu River in Beibu Gulf as an Example. *Front. Earth Sci.* **10**, (2022).

34. Liu, J. T. *et al.* Coupling between physical processes and biogeochemistry of suspended particles over the inner shelf mud in the East China Sea. *Mar. Geol.* **442**, (2021).

35. Renosh, P. R., Zhang, J., Sauzède, R. & Claustre, H. Vertically Resolved Global Ocean Light Models Using Machine Learning. *Remote Sens.* **15**, (2023).

36. Wei, G., Liu, Y., Li, X., Shao, L. & Liang, X. Climatic impact on Al, K, Sc and Ti in marine sediments: evidence from ODP site 1144, south China sea. *Geochem. J.* **37**, 593–602 (2003).

37. Delfino, F. A. A., Bevilaqua, D. & Benedetti, A. V. EIS studies of chalcopyrite involving iron(II) ions. *Solid State Phenom.* **262 SSP**, 496–500 (2017).

38. Kügler, S. *et al.* Iron-organic matter complexes accelerate microbial iron cycling in an iron-rich fen. *Sci. Total Environ.* **646**, 972–988 (2019).

39. Hudson, J. M., Luther, G. W., III & Chin, Y.-P. Assessing Iron Complexation by Dissolved Organic Matter Using Mediated Electrochemical Oxidation. *ACS Earth Space Chem.* **8**, 1810–1819 (2024).

40. Hassler, C. S., Simó, R., Fawcett, S. E., Ellwood, M. J. & Jaccard, S. L. Marine biogenic humic substances control iron biogeochemistry across the southern ocean. *Nat. Commun.* **16**, 2662 (2025).

41. Jones, R. L. *et al.* Antarctic glaciers export carbon-stabilised iron(II)-rich particles to the surface southern ocean. *Nat. Commun.* **16**, 5015 (2025).

42. Cutting, R. S., Coker, V. S., Fellowes, J. W., Lloyd, J. R. & Vaughan, D. J. Mineralogical and morphological constraints on the reduction of Fe(III) minerals by *Geobacter sulfurreducens*. *Geochim. Cosmochim. Acta* **73**, 4004–4022 (2009).

43. Yamashita, T. & Hayes, P. Analysis of XPS spectra of Fe^{2+} and Fe^{3+} ions in oxide materials. *Appl. Surf. Sci.* **254**, 2441–2449 (2008).

44. Yan, L. *et al.* Fast phase transformation of 2-line ferrihydrite to hematite as induced by the injection of photoelectrons. *Chem. Geol.* **690**, 122887 (2025).

45. Hettiarachchi, E. *et al.* Atmospheric processing of iron-bearing mineral dust aerosol and its effect on growth of a marine diatom, *cyclotella meneghiniana*. *Environ. Sci. Technol.* **55**, 871–881 (2021).

46. Ansari, A. A., Ansari, A. A., Abouhend, A. S., Gikonyo, J. G. & Park, C. Photogranulation in a Hydrostatic Environment Occurs with Limitation of Iron. *Environ. Sci. Technol.* **55**, 10672–10683 (2021).

47. Duan, R. *et al.* Contrasting responses of oceanic and coastal *SYNECHOCOCCUS* to iron limitation and warming interactions. *Environ. Microbiol. Rep.* **17**, e70158 (2025).

48. Kolody, B. C. *et al.* Nitrogen and iron availability drive metabolic remodeling and natural selection of diverse phytoplankton during experimental upwelling. *Msystems* **7**, e00729-22 (2022).

49. Burton, J. A. J., Edwards, M. J., Richardson, D. J. & Clarke, T. A. Electron transport across bacterial cell envelopes. *Annu. Rev. Biochem.* https://doi.org/10.1146/annurev-biochem-052621-092202 (2025)

doi:10.1146/annurev-biochem-052621-092202.

50. Shi, L. *et al.* Extracellular electron transfer mechanisms between microorganisms and minerals. *Nat. Rev. Microbiol.* **14**, 651–662 (2016).

51. Yang, B. *et al.* Spatio-temporal variations of chlorophyll a and primary productivity and its influence factors in Qinzhou Bay. *Huanjing Kexue XuebaoActa Sci. Circumstantiae* **35**, 1333–1340 (2015).

52. Chase, Z., Strutton, P. G. & Hales, B. Iron links river runoff and shelf width to phytoplankton biomass along the U.S. West Coast. *Geophys. Res. Lett.* **34**, (2007).

53. Kim, T.-W., Najjar, R. G. & Lee, K. Influence of precipitation events on phytoplankton biomass in coastal waters of the eastern United States. *Glob. Biogeochem. Cycles* **28**, 1–13 (2014).

54. Millero, F. J., Sotolongo, S. & Izaguirre, M. The oxidation kinetics of Fe(II) in seawater. *Geochim. Cosmochim. Acta* **51**, 793–801 (1987).

55. Santana-Casiano, J. M., González-Dávila, M. & Millero, F. J. Oxidation of nanomolar levels of Fe(II) with oxygen in natural waters. *Environ. Sci. Technol.* **39**, 2073–2079 (2005).

56. Schaedler *et al.* Microbially mediated coupling of Fe and N cycles by nitrate-reducing Fe (II)-oxidizing bacteria in littoral freshwater sediments. *Appl Env. Microbiol* **84**, e02013-17 (2018).

57. Zhong, C. *et al.* Photoelectron-promoted metabolism of sulphate-reducing microorganisms in substrate-depleted environments. *Environ. Microbiol.* **26**, e16683 (2024).

58. Drosos, M., Ren, M. & Frimmel, F. H. The effect of NOM to TiO_2: interactions and photocatalytic behavior. *Appl. Catal. B Environ.* **165**, 328–334 (2015).

59. Strickland, J. D. H. & Parsons, T. R. A practical handbook of seawater analysis, 2nd edition. https://repository.oceanbestpractices.org/handle/11329/1994 (1972).

60. Lafuente, B., Downs, R. T., Yang, H. & Stone, N. 1. The power of databases: the RRUFF project. in *Highlights in mineralogical crystallography* (eds Armbruster, T. & Danisi, R. M.) 1–30 (DE GRUYTER, 2015). doi:10.1515/9783110417104-003.

61. Shang, C. & Zelazny, L. W. Selective dissolution techniques for mineral analysis of soils and sediments. in *SSSA book series* (eds Ulery, A. L. & Richard Drees, L.) vol. 5 33–80 (Wiley, 2008).

62. Schwertmann, U. & Cornell, R. M. *Iron Oxides in the Laboratory: Preparation and Characterization*. (John Wiley & Sons, 2008).

63. Kester, D. R., Duedall, I. W., Connors, D. N. & Pytkowicz, R. M. Preparation of artificial seawater. *Limnol. Oceanogr.* **12**, 176–179 (1967).

64. Viollier, E., Inglett, P. W., Hunter, K., Roychoudhury, A. N. & Van Cappellen, P. The ferrozine method revisited: Fe(II)/Fe(III) determination in natural waters. *Appl. Geochem.* **15**, 785–790 (2000).

65. Thompson, M. *Handbook of Inductively Coupled Plasma Spectrometry: Second Edition*. (Springer Science & Business Media, 2012).

66. Liu, Y., Ding, H., Sun, Y., Li, Y. & Lu, A. Genome analysis of a marine bacterium *Halomonas* sp. and its role in nitrate reduction under the influence of photoelectrons. *Microorganisms* **8**, 1529 (2020).

67. ISO10304-1. Water quality — determination of dissolved anions by liquid chromatography of ions — part 1: determination of bromide, chloride, fluoride, nitrate, nitrite, phosphate and sulfate. (2007).

68. Packard, T. T., Healy, M. L. & Richards, F. A. Vertical distribution of the activity of the respiratory electron transport system in marine plankton1. *Limnol. Oceanogr.* **16**, 60–70 (1971).

69. Walton, G. M., Bertics, P. J., Hudson, L. G., Vedvick, T. S. & Gill, G. N. A three-step purification procedure for protein kinase C: characterization of the purified enzyme. *Anal. Biochem.* **161**, 425–437 (1987).

70. R Core Team. *R: A Language and Environment for Statistical Computing*. (R Foundation for Statistical Computing, Vienna, Austria, 2020).

Funding

This work was funded by the National Natural Science Foundation of China (Grant No. 42192502, Grant No. 92251301, Grant No. 91851208 and Grant No. 41820104003).

Author Contributions Statement

T.L. and H.D. contributed equally to this work. A.L. conceived and supervised the project. T.L. and H.D. designed experiments and analyzed data. T.L. also performed field sampling. L.M. and X.G. conducted photochemical experiments and mineral characterization. Y. Liu performed bio-electrochemical experiments. F.Z., S.Y., and Q.Y. performed field sampling and sample processing. Y. Li and C.W. contributed to data interpretation. J.L. contributed to discussions on iron mineral transformations. S.J. contributed to data interpretation. T.L., H.D., and A.L. wrote the manuscript with input from all authors.

Competing Interests Statement

The authors declare no competing interests.

Figure Captions

Figure 1 **Distribution, composition, and photoelectric properties of suspended mineral particles in the Beibu Gulf (summer 2023 cruise). a**, Sampling sites in the Beibu Gulf, northern South China Sea, China. The Nanliu River and major tributaries are labeled. **b**, Spatial distribution of suspended particulate matter (SPM) concentration (mg L^{-1}). Estuarine waters (mean 4.5 mg L^{-1}) showed significantly higher concentrations than offshore waters (mean 1.2 mg L^{-1}). **c**, Bulk mineralogical composition determined by X-ray diffraction (XRD), showing the dominant phases of quartz, feldspar, and clay minerals.. **d**, Raman mapping of a representative particle aggregate showing spatial co-occurrence of iron oxides and titanium dioxide. **e**, Chopped-light chronoamperometry of natural suspended particle electrodes (red), non-semiconductor controls including quartz and clay (blue), and blank fluorine-doped tin oxide (FTO) electrodes (grey), demonstrating a significant and stable photocurrent response in the natural particle electrodes. **f**, Chopped-light chronoamperometry comparing photo-response of natural particle electrodes with pure mineral electrodes (anatase, hematite, and rutile) and non-semiconductor controls (quartz, clay).

Figure 2 **Anatase photocatalysis enhances dissolution of synthetic iron minerals and Fe(II) production. a**, Time course of dissolved Fe(II) release from goethite (Gt) and lepidocrocite (Lpc) in artificial seawater under dark and illuminated conditions without anatase. **b**, Time course of Fe(II) release from lepidocrocite under four conditions: with or without anatase (Ant, 0.1 g L^{-1}), under dark or illuminated conditions, in artificial seawater without added dissolved organic matter (DOM). **c**, Same experimental design as **b**, but with oxalate (200 μM) added to all treatments as a model DOM ligand; note the higher Fe(II) concentrations (y-axis scale) compared to **b**. **d**, Proportion of Fe(II) in total dissolved Fe (%) by the end of the experiment for four synthetic iron minerals, ferrihydrite (Fh), lepidocrocite (Lpc), goethite (Gt), and hematite (Hem), under four conditions: dark, light, light + anatase, and light + anatase + oxalate. **e**, First-derivative diffuse reflectance spectra of lepidocrocite before reaction (pristine) and after 12-day reaction under light + anatase conditions. **f**, High-resolution Fe 2*p* X-ray photoelectron spectroscopy (XPS)

of lepidocrocite after reaction under light + anatase conditions, with peak deconvolution showing Fe(II) component at 715.2 eV (arrow) alongside Fe(III). **g**, Schematic of proposed photocatalytic mechanism at anatase-Fe(III) oxide heterojunctions.

Figure 3 **Microbial responses to photoelectrochemical conditions and field observations of phytoplankton distribution. a - f**, Laboratory experiments. **a**, Bacterial abundance as a function of applied cathode potential in photoelectrochemical cultures. Origin, initial inoculum; 0, open circuit potential (OCP, control). **b**, Time course of nitrate reduction by *Halomonas* sp. under different applied potentials (V vs. Ag/AgCl electrode). **c**, Time course of nitrate reduction by *Bacillus tropicus* under illumination (300 - 800 nm, 100 mW cm^{-2}) with minerals: abiotic control, anatase alone (Ant), biotic control (no minerals), and anatase + lepidocrocite (Ant + Lpc). **d**, Time course of sulfate reduction by sulfate-reducing bacteria (SRB) enrichment culture under different applied potentials. **e**, Electron transfer system activity (ETSA) of *Halomonas* sp. at days 0, 10, and 20 under different potentials. **f**, Cytochrome c (Cyt c) content (intracellular and membrane fractions) in *Halomonas* sp. under different potentials. **g**, Field observations from the Beibu Gulf (summer 2023): chlorophyll *a* concentration (mg m^{-3}) at the surface (left) and near-bottom (right).

Figure 4 **Conceptual model of semiconductor mineral photocatalysis in the euphotic zone.** Terrigenous and atmospheric inputs supply photoactive semiconductor minerals (anatase, Fe(III) oxides) to the sunlit ocean. Under solar irradiation, anatase-Fe(III) oxide heterojunctions generate photoelectrons that reduce Fe(III) to Fe(II), producing a flux of bioavailable iron. This Fe(II) can be: (i) directly assimilated by phytoplankton; (ii) re-oxidized to Fe(III), completing the redox cycle; or (iii) utilized as an electron donor by denitrifying and sulfate-reducing bacteria (SRB), coupling iron cycling to nitrogen (N) and sulfur (S) biogeochemistry. Right panel shows conceptual water column profiles of O_2, light, NO_3^-, Fe(III), and Fe(II), reflecting general vertical gradients. *hv*, photon energy; e^-, photoelectron; h^+, photogenerated hole.

Editor's Summary

Semiconductor mineral photocatalysis, previously shown to operate via iron-oxide coatings on Earth's land surface, is extended to the sunlit ocean, where anatase and iron oxides drive Fe(III)-to-Fe(II) cycling and supply bioavailable iron.

Peer review information: *Nature Communications* thanks Marios Drosos and the other, anonymous, reviewer(s) for their contribution to the peer review of this work. A peer review file is available.

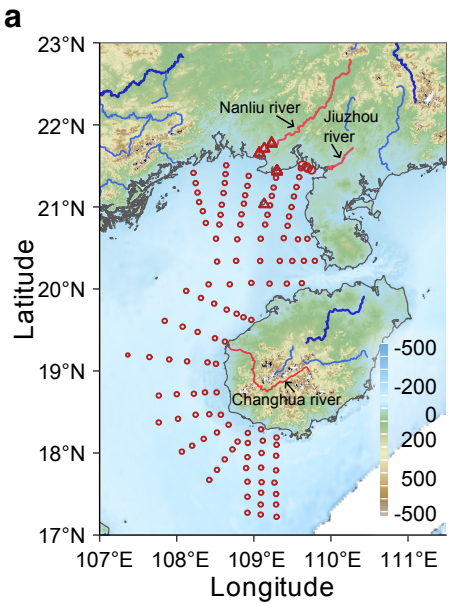
a
Nanliu river
Jiuzhou river
Changhua river
Latitude
Longitude
23°N
22°N
21°N
20°N
19°N
18°N
17°N
107°E
108°E
109°E
110°E
111°E
-500
-200
0
200
500
-500

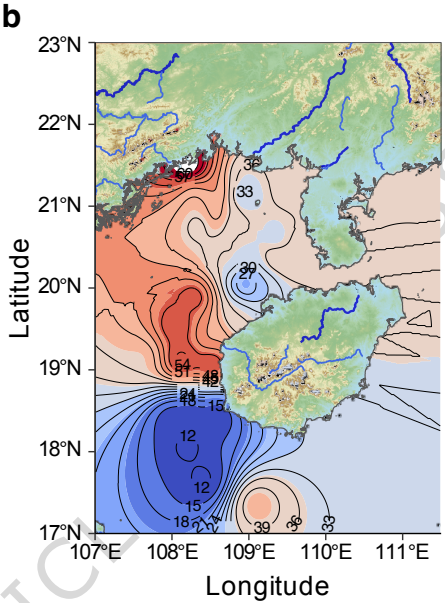
b
Latitude
Longitude
23°N
22°N
21°N
20°N
19°N
18°N
17°N
107°E
108°E
109°E
110°E
111°E

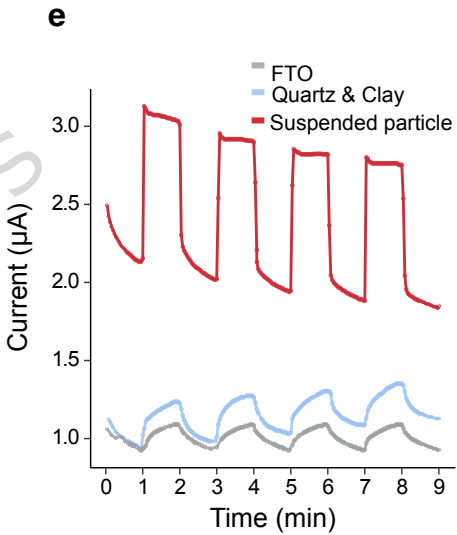
e
FTO
Quartz & Clay
Suspended particle
Current (μA)
Time (min)

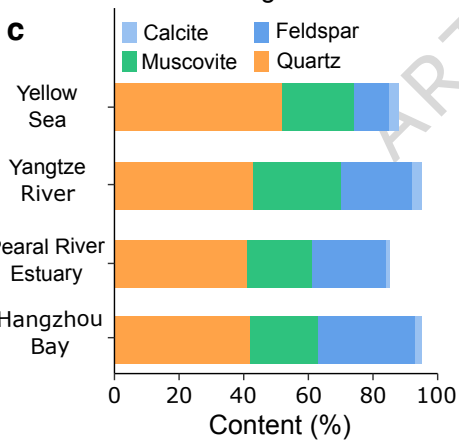
c
Calcite
Feldspar
Muscovite
Quartz
Yellow Sea
Yangtze River
Pearal River Estuary
Hangzhou Bay
Content (%)

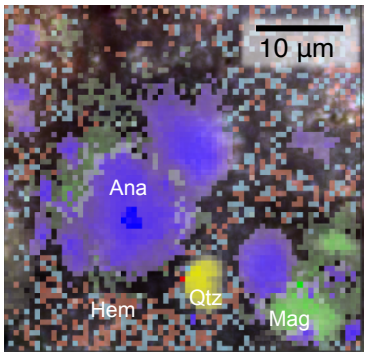
d
10 μm
Ana
Hem
Qtz
Mag

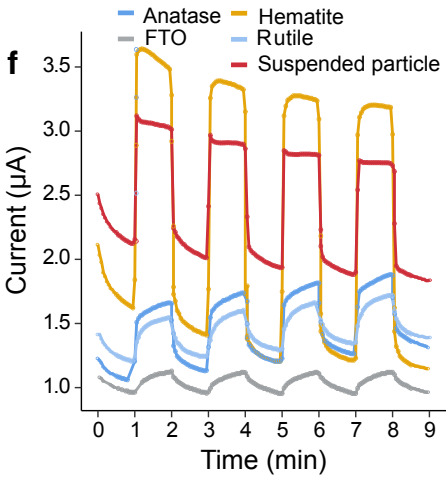
f
Anatase
Hematite
FTO
Rutile
Suspended particle
Current (μA)
Time (min)

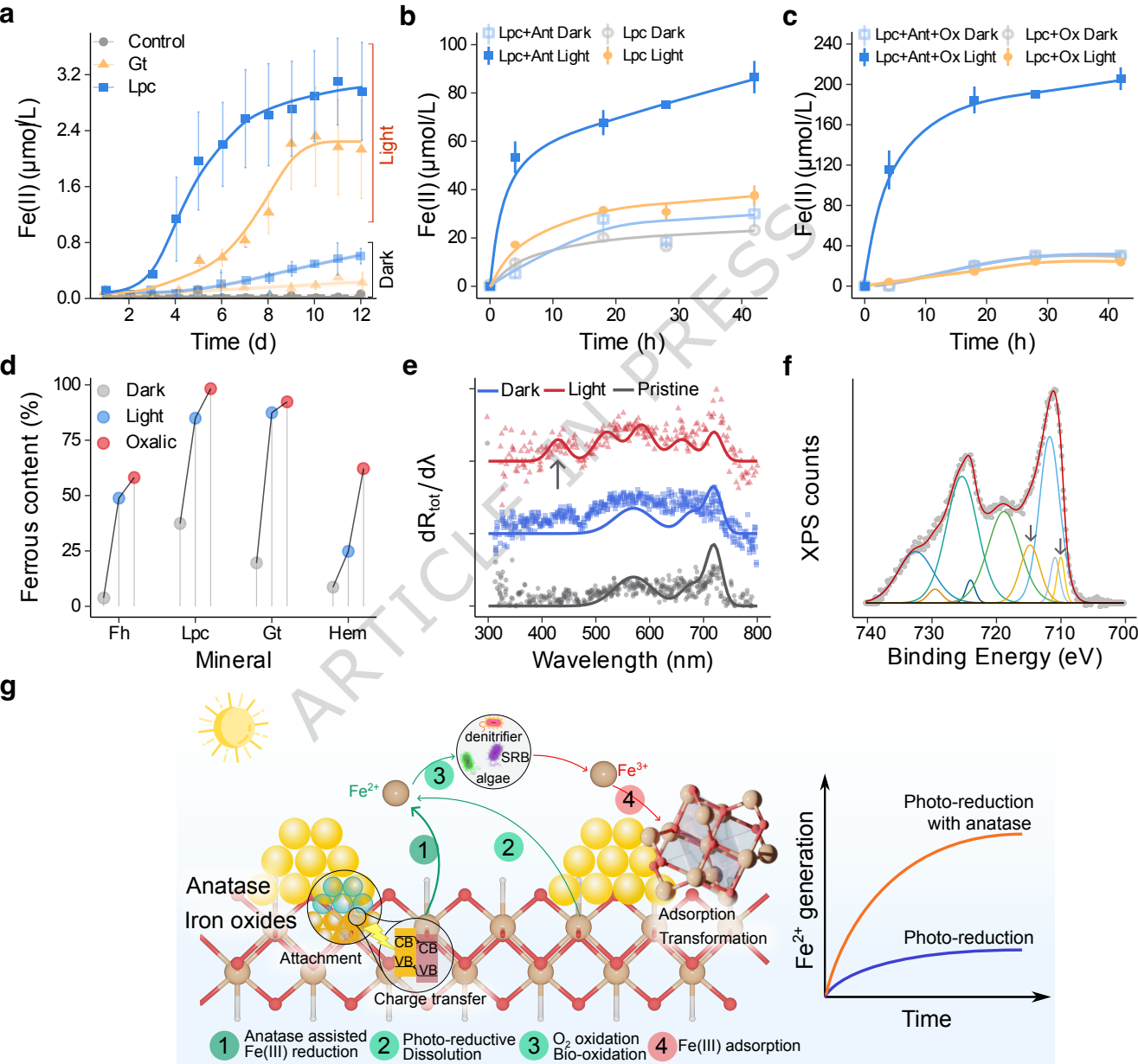
a
Control
Gt
Lpc
Light
Dark
Fe(II) (μmol/L)
Time (d)
b
Lpc+Ant Dark
Lpc+Ant Light
Lpc Dark
Lpc Light
Fe(II) (μmol/L)
Time (h)
c
Lpc+Ant+Ox Dark
Lpc+Ant+Ox Light
Lpc+Ox Dark
Lpc+Ox Light
Fe(II) (μmol/L)
Time (h)
d
Dark
Light
Oxalic
Ferrous content (%)
Fh
Lpc
Gt
Hem
Mineral
e
Dark
Light
Pristine
dR_tot/dλ
Wavelength (nm)
f
XPS counts
Binding Energy (eV)
g
denitrifier
SRB
algae
Fe2+
Fe3+
Anatase
Iron oxides
Attachment
CB
VB
Charge transfer
Adsorption
Transformation
1 Anatase assisted Fe(III) reduction
2 Photo-reductive Dissolution
3 O2 oxidation Bio-oxidation
4 Fe(III) adsorption
Photo-reduction with anatase
Photo-reduction
Fe2+ generation
Time

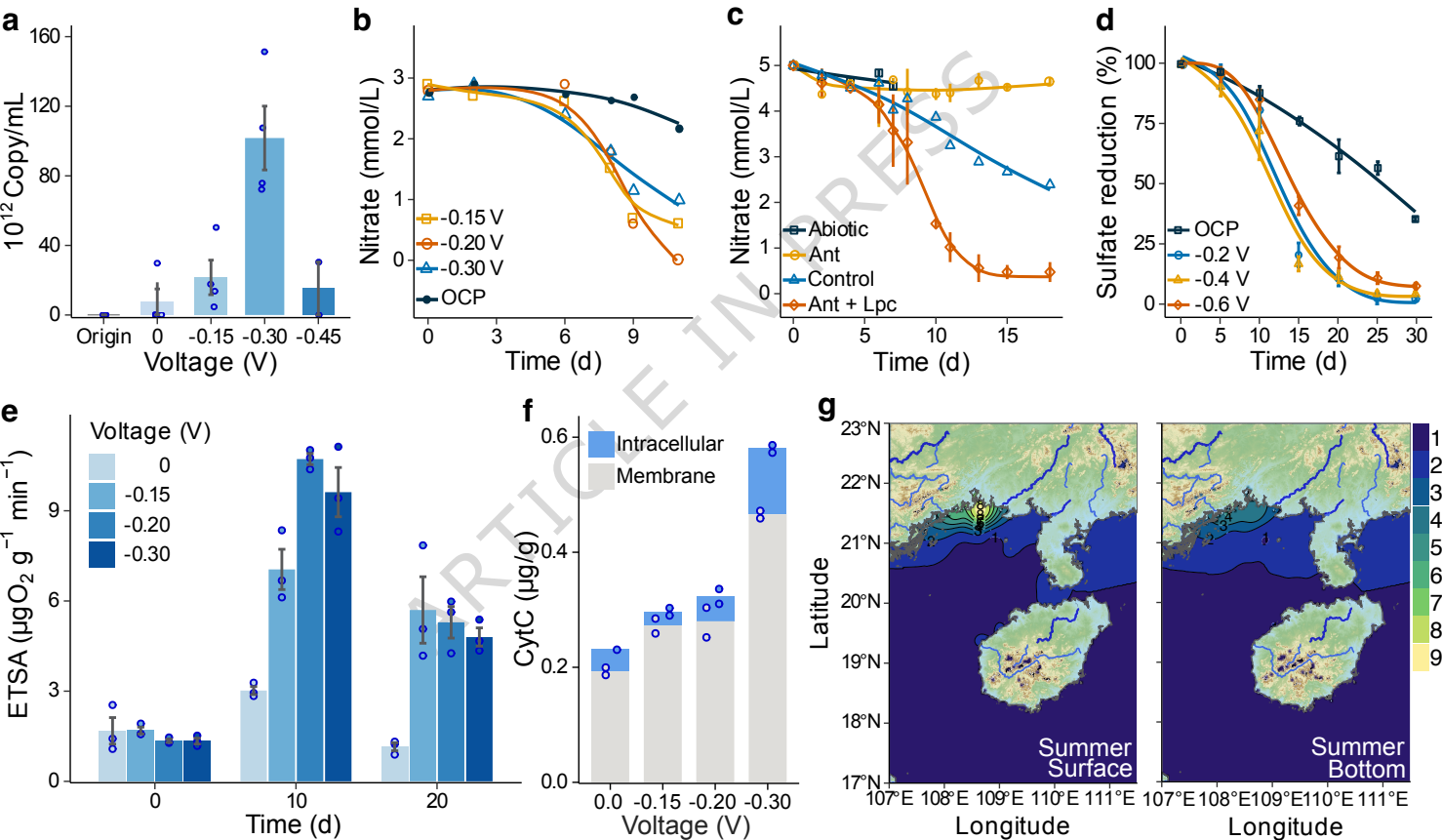

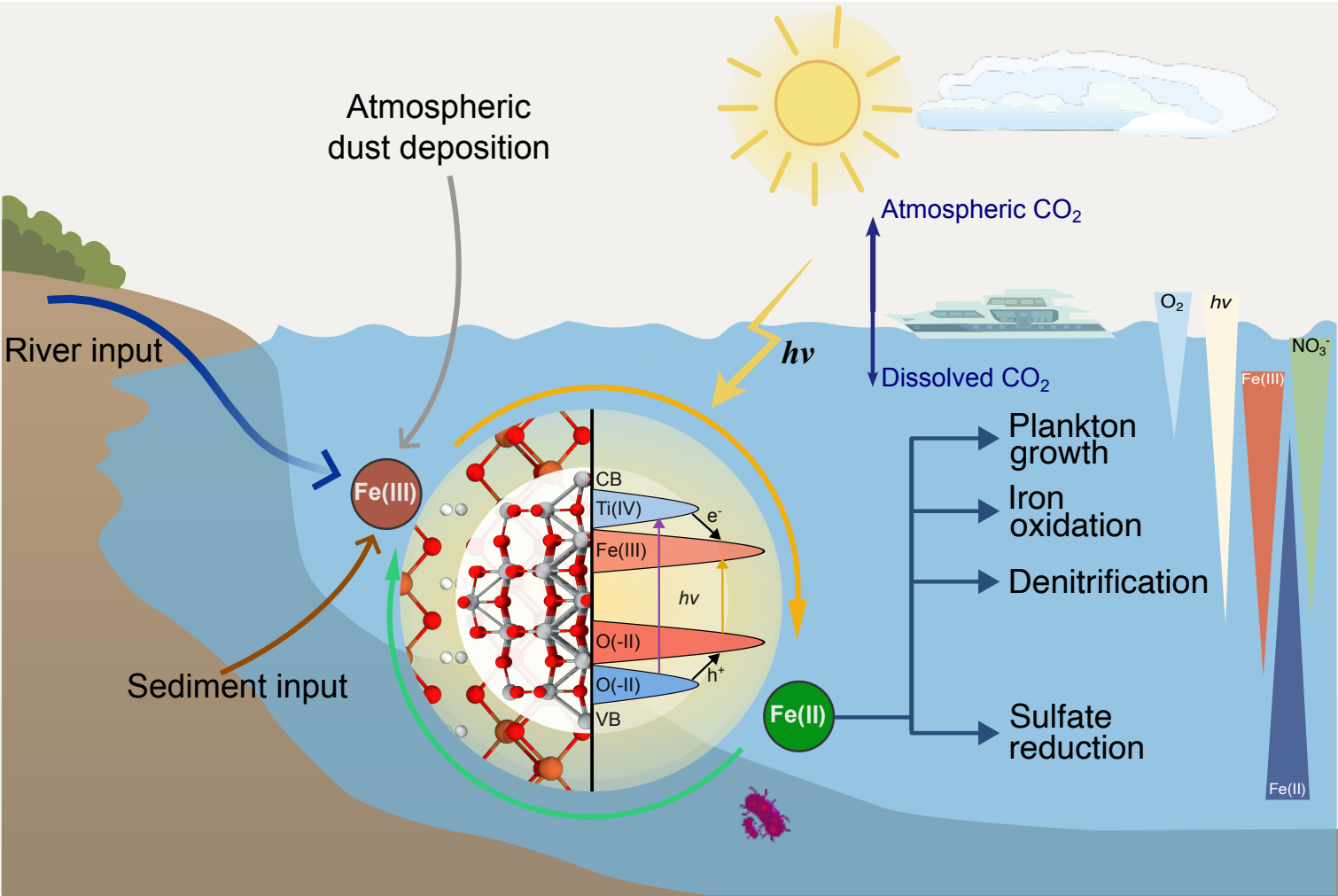
Atmospheric
dust deposition
Atmospheric CO_2
Dissolved CO_2
River input
Sediment input
hv
Fe(III)
CB
Ti(IV)
e⁻
Fe(III)
hv
O(-II)
h⁺
O(-II)
VB
Fe(II)
Plankton
growth
Iron
oxidation
Denitrification
Sulfate
reduction
O_2
hv
NO_3^-
Fe(III)
Fe(II)